Tumour subregion analysis of colorectal liver metastases using semi-automated clustering based on DCE-MRI: comparison with histological subregions and impact on pharmacokinetic parameter analysis

Authors:

James M Franklin MB BS MA (Cantab.) MRCP FRCR DPhil[1,2], Benjamin Irving MSc PhD[3], Bartlomiej W Papiez PhD[3], Jesper F Kallehauge PhD[3], Lai Mun Wang MB BCh MRCP FRCPath[4], Robert D Goldin MD FRCPath[5], Adrian L Harris MB ChB MA DPhil FRCP[6], Ewan M Anderson BM BCh FRCR[7], Julia A Schnabel PhD MSc[3,8], Michael A Chappell DPhil MEng[3], Michael Brady PhD[6], Ricky A Sharma MA MB BChir FRCP FRCR PhD[9], Fergus V Gleeson MB BS FRCP FRCR[7]

Affiliations:

1. Institute of Medical Imaging and Visualisation, Bournemouth University, UK
2. Radiology Department, Royal Bournemouth and Christchurch Hospitals NS Foundation Trust, UK
3. Institute of Biomedical Engineering (Department of Engineering Science), University of Oxford, UK
4. Department of Cellular Pathology, Oxford University Hospitals NHS Foundation Trust, UK
5. Centre for Pathology, Imperial College, London, UK
6. Department of Oncology, University of Oxford, UK
7. Radiology Department, Churchill Hospital, Oxford University Hospitals NHS Foundation Trust, UK
8. School of Biomedical Engineering and Imaging Sciences, King's College London, UK
9. NIHR University College London Hospitals Biomedical Research Centre, UCL Cancer Institute, University College London, UK

Corresponding Author:

Dr James Franklin

Institute of Medical Imaging and Visualisation, Royal London House, Bournemouth University, Bournemouth, BH1 3LT

Email: jfranklin@bournemouth.ac.uk

Tel: 00 44 01202 964765

Joint First Authorship:

This was a multidisciplinary study which drew on a range of expertise from radiology, computational engineering, oncology and pathology. Dr James Franklin and Dr Benjamin Irving have contributed equally to this paper and request to be recognised as dual first authors in the event of acceptance for publication. Dr James Franklin, a Radiologist, established the prospective trial and was responsible for designing and coordinating the research imaging and histological analyses. Dr Benjamin Irving, an Engineering Scientist, developed the methodology and software for performing the tumour subregion analysis.

Contact Details:

BI

Institute of Biomedical Engineering, Department of Engineering Science, Old Road Campus Research Building, Roosevelt Drive, Oxford, OX3 7DQ

Email: benjamin.irving@eng.ox.ac.uk

Tel: 00 44 1865 617657

BWP

Institute of Biomedical Engineering, Department of Engineering Science, Old Road Campus Research Building, Roosevelt Drive, Oxford, OX3 7DQ

Email: bartlomiej.papiez@eng.ox.ac.uk

Tel: 00 44 1865 617657

JK

Institute of Biomedical Engineering, Department of Engineering Science, Old Road Campus Research Building, Roosevelt Drive, Oxford, OX3 7DQ
Email: jespkall@rm.dk

LMW
Department of Cellular Pathology John Radcliffe Hospital, Headley Way, Oxford OX3 9DU
Email: laimun.wang@ouh.nhs.uk

RG
Department of Cellular Pathology, Clarence Wing, St Mary's Campus, Praed St, London W2 1NY
Email: r.goldin@imperial.ac.uk
Tel: 00 44 2033 121305

ALH
Department of Oncology, Old Road Campus Research Building, Roosevelt Drive, Oxford, OX3 7DQ
Email: adrian.harris@oncology.ox.ac.uk
Tel: 00 44 1865 222457

EMA
Department of Radiology, Churchill Hospital, Oxford OX3 7LE
Email: ewan.anderson@ouh.nhs.uk
Tel: 00 44 1865 245746
Fax: 00 44 1865 235005

JAS
School of Biomedical Engineering and Imaging Sciences, 4th Floor, Lambeth Wing, St Thomas’ Hospital, London SE1 7EH, UK
Tel: 00 44 2071 888369
E-mail: julia.schnabel@kcl.ac.uk

MAC
Institute of Biomedical Engineering, Department of Engineering Science, University of Oxford, Old Road Campus Research Building, Oxford, OX3 7DQ
Email: michael.chappell@eng.ox.ac.uk
Tel: 00 44 1865 617657

MB
Department of Oncology, Old Road Campus Research Building, Roosevelt Drive, Oxford, OX3 7DQ
Email: mike.brady@oncology.ox.ac.uk
Tel: 00 44 1865 617346

RAS
NIHR University College London Hospitals Biomedical Research Centre, UCL Cancer Institute, University College London, 72 Huntley Street, London WC1E 6DD
Email: g.bull@ucl.ac.uk
Tel: 00 44 2031 082212

FVG
Department of Radiology, Churchill Hospital, Oxford OX3 7LE
Email: fgleeson@mac.com
Tel: 00 44 1865 245746
Fax: 00 44 1865 235005

Authorship:

All authors have materially participated in the research and/or article preparation. JMF, EMA and FVG are radiologists who were involve in study design imaging protocols, study design and article preparation; RG and LMW are histopathologists involved in histopathological preparation, analysis and article preparation; RS is an oncologist involved in patient recruitment and article preparation; ALH is an oncologist involved in article preparation; BI, BWP, JK, MAC, JAS and MB are engineers who performed or supervised the image analysis and were involved in article preparation. All authors have approved the final article.

Funding:

This study was funded by the Oxford Health Sciences Research Committee (Grant Reference 955) and by CRUK and EPSRC Cancer Imaging Centre in Oxford (Programme Grant C5255/A16466). RAS is supported by the National Institute for Health Research University College London Hospitals Biomedical Research Centre, the Cancer Research UK University College London Experimental Cancer Medicine Centre, and the Cancer Research UK Centers Network Accelerator Award Grant (A21993) to the ART-NET Consortium.

Disclosures:

RAS declares consultancy with Affidea, Astra Zeneca, Boston Scientific, BTG, Cancer Research Technology, DeepMind, Eisai, Sirtex, Terumo and Varian. The remaining authors (James M Franklin, Benjamin Irving, Bartlomiej W Papiez, Jesper F Kallehauge, Lai Mun Wang, Robert D Goldin, Adrian L Harris, Ewan M Anderson, Julia A Schnabel, Michael A Chappell, Michael Brady, Fergus V Gleeson) declare no conflicts of interested related to this publication.

IRB Approval:

This prospective study received appropriate formal ethical approval.

Type of Article:

Original Research

Tumour subregion analysis of colorectal liver metastases using semi-automated clustering based on DCE-MRI: comparison with histological subregions and impact on pharmacokinetic parameter analysis

Abstract

Purpose

To use a novel segmentation methodology based on dynamic contrast-enhanced magnetic resonance imaging (DCE-MRI) to define tumour subregions of liver metastases from colorectal cancer (CRC), to compare these with histology, and to use these to compare extracted pharmacokinetic (PK) parameters between tumour subregions.

Materials and Methods

This ethically-approved prospective study recruited patients with CRC and ≥1 hepatic metastases scheduled for hepatic resection. Patients underwent DCE-MRI pre-metastasectomy. Histological sections of resection specimens were spatially matched to DCE-MRI acquisitions and used to define histological subregions of viable and non-viable tumour. A semi-automated voxel-wise image segmentation algorithm based on the DCE-MRI contrast-uptake curves was used to define imaging subregions of viable and non-viable tumour. Overlap of histologically-defined and imaging subregions was compared using the Dice similarity coefficient (DSC). DCE-MRI PK parameters were compared for the whole tumour and histology-defined and imaging-derived subregions.

Results:

Fourteen patients were included in the analysis. Direct histological comparison with imaging was possible in nine patients. Mean DSC for viable tumour subregions defined by imaging and histology was 0.738 (range 0.540-0.930). There were significant differences between K^{trans} and k_{ep} for viable and non-viable subregions ($p<0.001$) and between whole lesions and viable subregions ($p<0.001$).

Conclusion:

We demonstrate good concordance of viable tumour segmentation based on pre-operative DCE-MRI with a post-operative histological gold-standard. This can be used to extract viable tumour-specific values from quantitative image analysis, and could improve treatment response assessment in clinical practice.

Keywords

Liver Neoplasm;

Colorectal Neoplasm;

MRI;

Perfusion Imaging.

Abbreviations

CRC – colorectal cancer

CRLM – colorectal liver metastases

DCE-MRI – dynamic contrast enhanced MRI

IB – imaging biomarkers

PK – pharmacokinetic

RECIST – response evaluation criteria in solid tumours

ROI – region of interest

VOI – volume of interest

Introduction

Colorectal cancer (CRC) is the fourth most common cancer in the UK[1] and US[2]. Colorectal liver metastases (CRLM) complicate approximately 25% of cases of CRC, either at the time of presentation or during follow-up.[3,4] CRLM are pathologically heterogeneous, comprising regions of viable, cellular tumour as well as areas of predominantly acellular fibrosis and necrosis. For patients with CRC, primary and metastatic lesions may also contain mucinous regions and areas of calcification.[5]

Cellular regions of tumour have different MRI characteristics from other components,[6] and could be used as the basis for tumour subsegmentation. Segmenting viable tumour regions using *in vivo* imaging could have substantial clinical utility. Firstly, it may assist in assessing response to treatment: conventional size-based response criteria such as RECIST 1.1[7] assume that all treatment response is associated with changes in tumour size; incorporating morphological response criteria can improve response assessment in some settings.[8] Secondly, in patients with CRLM, pathological assessment of viable tumour[9,10] and the composition of the metastasis[11] are prognostically relevant. However, there is no reliable methodology to quantify this *in vivo*, where it could be used to influence clinical decision-making.

Segmentation of viable tumour regions by imaging also has the potential to improve analysis of quantitative imaging data. Extraction of quantitative imaging biomarkers (IB) has typically been based on analysis of the whole lesion, which includes acellular regions, as well as the regions of viable tumour. When analysing pharmacokinetic (PK) data derived from, for example, dynamic contrast-enhanced MRI (DCE-MRI), it may be preferable to focus on regions of viable tumour. This could improve on the variable associations found between perfusion imaging and histological parameters observed to date,[12,13] and improve tumour phenotyping by imaging. Finally, manual delineation of tumour subregions for pharmacokinetic (PK) analysis introduces intra-observer variability,[14,15] and may be impractical in clinical practice, and therefore automated or semi-automated segmentation is preferred.

We developed a methodology to semi-automatically segment tumour and non-tumour regions based on DCE-MRI characteristics. This study has two aims: firstly, to compare these subregions with a reference standard of histological subregions from spatially matched resected CRLM and, secondly, to analyse the impact of using these tumour subregions to examine DCE-MRI-derived PK data.

Methods and Materials

Patients

Patients were eligible for this ethically approved prospective observational study if they had a diagnosis of CRC, at least one hepatic metastasis ≥8mm not previously treated with systematic chemotherapy and were scheduled for surgical liver metastasectomy. All patients provided written informed consent to the study procedures. DCE-MRI of the liver was performed at baseline and then patients either proceeded directly to surgery, or were treated with neoadjuvant chemotherapy as part of their routine clinical care. To minimise changes to tumour morphology between pre-operative imaging and histopathological assessment, patients were excluded from the imaging-histopathology correlation analysis if the interval between DCE-MRI and surgery exceeded 28 days.

DCE-MRI technique

MRI studies were performed at 1.5T (GE HDX Twinspeed MR scanner; GE, Milkwaukee, WI) with an 8-channel torso coil. All DCE-MRI imaging was performed in the axial plane. A multiparametric MRI incorporating T2 weighted (T2W), T1 weighted (T1W), diffusion weighted (DWI) and DCE-MRI was performed. DCE-MRI was performed using multiple flip-angle (15°,9° and 3°) sequences to calculate voxel $T1_0$ values followed by T1W imaging (axial 3D multiphase LAVA (imaging options: Fast, ZIP2 Asset), acceleration factor = 1.00, field of view = 42, phase FOV = 0.8, matrix 320 x 192, slice thickness = 5.0 mm, pixel size = 1.31 x 1.75 x 5 mm, location per slab = 22, overlap = 0, TR = 4.46 s, TE = 2.128 s) of a predefined volume centered on the largest liver metastasis before and after the injection of a 15 mL bolus of gadolinium chelate (Gadoteridol; ProHance, Bracco Diagnostics, Princeton, USA), with a 15 mL saline flush. Volumes were acquired over a 7s breath-hold during end-expiration for at least 7 minutes after contrast administration, with lengthening interscan intervals (0-2 minutes – 1 breath cycle between each acquisition; 2-4 minutes: 2 breath cycles between each acquisition; 4-6 minutes: 3 breath cycles between each acquisition; 6+ minutes: 4 breath cycles between each acquisition). All studies had at least 20 acquisitions to inform the PK-modelling.

Histopathological cut-up and staining

At the time of hepatic resection the specimen was oriented perpendicular to the craniocaudal axis and the anterior surface marked. The midpoint of the metastasis in the craniocaudal axis was identified using *ex-vivo* ultrasound and marked superficially on the specimen. For deep lesions, an ultrasound examination was performed at the time of histological cut-up.

Histopathological cut-up was performed prior to formalin fixation. Liver specimens were sectioned in the axial plane at the meridian of the selected metastasis based on the surgical and sonographic landmarks, with further approximately five millimeter sections taken through the metastasis. The sections were marked (anterior, posterior, medial and lateral), photographed, and then transferred to cassettes. Sections were fixed overnight in formalin and embedded in paraffin. Three micrometer sections of each metastasis at the midpoint section were cut and stained using haematoxylin and eosin (H&E), and mounted on glass slides.

Histopathological analysis

H&E stained slides were reviewed, using light microscopy, jointly by two consultant histopathologists with >10 years experience in reporting CRC histopathology. Each metastasis was scored by consensus, blinded to all clinical and imaging data, for the percentage of four principal components of CRLM: viable tumour, fibrosis, necrosis and mucin to the nearest 5%. This was used to determine proportion of viable tumour estimate by visual assessment.

Image-histopathology alignment

Histopathology slides were scanned digitally (Aperio CS2 Slidescanner, Leica Biosystems, USA) and imported into OsiriX 2 DICOM Viewer (Pixmeo SARL, Bernex, Switzerland) as converted DICOM files (JPEG to DICOM v2.0). DCE-MRI studies were also imported. Histopathological images were scaled to match the tumour on MRI to allow for size reduction during formalin fixation: the entire lesion was manually measured in the longest axial plane (x-dimension) and in the longest perpendicular (y-dimension) at both imaging and histopathology. The histopathology images were then rescaled to match the x- and y-dimensions of the lesion on MRI.

Histopathological images were fused with the DCE-MRI 4D volume and manually aligned to match the lesion contour in the imaging space, based on the histopathological orientation and local features such as the liver capsule or local blood vessels.

Lesion subregion derivation

The entire metastatic lesion ($\mathrm{ROI}_{\text{lesion-histopathology}}$) and the subregion(s) of viable tumour ($\mathrm{ROI}_{\text{viable-histopathology}}$) were manually delineated on the histopathology image, and saved in the imaging space (Figure 1). $\mathrm{ROI}_{\text{viable-histopathology}}$ encompassed regions of predominantly viable, cellular tumour. Non-contiguous tumour regions less than 500 µm in diameter were not included. To derive the non-viable tumour ROI ($\mathrm{ROI}_{\text{non-viable-histopathology}}$), the $\mathrm{ROI}_{\text{viable-histopathology}}$ was subtracted from $\mathrm{ROI}_{\text{lesion-histopathology}}$.

The whole volume of the metastatic lesion ($\mathrm{VOI}_{\text{lesion-imaging}}$) was manually delineated on the unenhanced T1W images, or, in cases where the lesion was better defined or larger, using the T2W images, by a radiologist with seven years' experience reporting liver MRI.

The imaging subregion analysis was performed using in-house software. To create the image-derived subregions the contrast uptake curves for the voxels within $\mathrm{VOI}_{\text{lesion-imaging}}$ and $\mathrm{ROI}_{\text{lesion-histopathology}}$ were analysed using a principal component analysis (PCA) of the DCE-MRI enhancement curves, followed by k-means clustering of these modes, as described in a prior publication.[16] Based on a retrospective analysis of the dataset, three PCA modes were found to capture the variation in the data, and best separate regions of different contrast uptake characteristics, and were used to automatically define four subregions. These four subregions were subsequently manually merged into two regions: viable tumour, identified by a wash-in/wash-out curve, and non-viable tumour, where there were other contrast curves (non-enhancing or contrast accumulation; Figure 2) as described by Kuhl *et al*.[17]

Thus for the $VOI_{lesion\text{-}imaging}$ two regions were defined: $VOI_{viable\text{-}imaging\text{-}subregion}$ and $VOI_{nonviable\text{-}imaging\text{-}subregion}$. Two regions were also defined within $ROI_{lesion\text{-}histopathology}$: $ROI_{viable\text{-}imaging\text{-}subregion}$ and $ROI_{nonviable\text{-}imaging\text{-}subregion}$.

DCE-MRI analysis

There were three stages to derivation of the PK parameters from DCE-MRI:

i. Motion correction

The liver is subject to respiratory motion. Although images were acquired in end expiration, which minimizes inter-frame motion (Kimura *et al,* 2004[18]), there was residual inter-frame motion. This was corrected using a non-rigid motion correction algorithm developed using liver DCE-MRI studies as we have previously described, which results in significant improvement in the registration error.[19]

ii. PK analysis

The variable flip angle sequence was registered to the baseline image of the DCE-MRI image and used to derive baseline T1 values ($T1_0$) and, for each voxel in the DCE-MRI acquisition, signal was converted to contrast concentration. The Toft's model, using population-average portal venous and arterial input functions[20], was fitted to the contrast enhancement curve of each voxel to produce maps of PK parameters.

iii. Extraction of PK parameters

The PK parameter maps were imported into proprietary in-house PK View software, which was developed to aid this analysis.[16] Mean, median, deviation, minimum and maximum values for K^{trans}, k_{ep} and $T1_0$ for each of the defined ROIs and VOIs were derived.

Data Analysis

i. Comparison of image-derived and histopathology defined subregions

To assess the agreement between regions defined on histopathology with those semi-automatically determined from imaging, the spatial overlaps of $ROI_{lesion\text{-}imaging}$ and $ROI_{lesion\text{-}histopathology}$, and $ROI_{viable\text{-}imaging\text{-}subregion}$ and $ROI_{viable\text{-}histopathology}$ were estimated using the Dice similarity coefficient (DSC)[21], as shown in Figure 3).

ii. Assessment of viable tumour

The percentage of viable tumour for the whole histopathology slide was reported by visual assessment by agreement of two consultant histopathologists. The percentage of viable tumour within the histopathology ROI and imaging ROI and VOI image were calculated:

- Histopathology: $100 * ROI_{viable\text{-}histopathology}/ROI_{lesion\text{-}histopathology}$
- ROI imaging $100 * ROI_{viable\text{-}imaging}/ROI_{lesion\text{-}imaging}$
- VOI imaging $100 * VOI_{viable\text{-}imaging}/VOI_{lesion\text{-}imaging}$

These values were correlated using the Pearson product-moment correlation coefficient.

iii. PK data analysis

$T1_0$ and PK parameters were summarized for each of the ROI/VOIs and presented graphically. The following $T1_0$ PK parameters comparisons were performed using paired Student’s T-test. p-values of <0.05 were taken to be significant.

To compare viable tumour subregions defined by imaging and defined by histopathology:

1) $ROI_{viable\text{-}imaging\text{-}subregion}$ and $ROI_{viable\text{-}histopathology}$

To compare viable tumour subregions defined by imaging in 2D and in 3D:

2) $ROI_{viable\text{-}imaging\text{-}subregion}$ and $VOI_{viable\text{-}imaging\text{-}subregion}$

To compare viable and non-viable subregions:

3) $ROI_{viable\text{-}histopathology}$ and $ROI_{nonviable\text{-}histopathology}$
4) $VOI_{viable\text{-}imaging\text{-}subregion}$ and $VOI_{nonviable\text{-}imaging\text{-}subregion}$

To compare the whole lesion with only the viable component:

5) $VOI_{lesion\text{-}imaging\text{-}subregion}$ and $VOI_{viable\text{-}imaging\text{-}subregion}$

Results

Patients

Fifteen patients were recruited to this prospective study. One patient was withdrawn. The remaining fourteen underwent hepatic metastasectomy. Of these fourteen patients, ten patients proceeded directly to metasectomy and four patients were treated with neoadjuvant chemotherapy. One patient declined post-treatment DCE-MRI, otherwise DCE-MRI was performed successfully in all cases at baseline and after chemotherapy where appropriate; and this provided the study dataset. Direct histological comparison with imaging was possible in nine patients: eight patients not treated with neoadjuvant chemotherapy and in one patient (patient 010) treated with neoadjuvant chemotherapy. One patient declined post-treatment DCE-MRI, one had further chemotherapy after post-treatment DCE-MRI, the specimen was not available for one patient, and one patient treated with chemotherapy had a complete pathological response at the time of resection, precluding direct assessment of imaging and histology. In one patient there was recurrence at a prior resection margin, with multiple small tumour islands, which it was not possible to co-register reliably with the DCE-MRI images.

Histopathology analysis

Viable tumour and non-viable subregions were defined for all patients as described above (see Figure 1).

Image analysis

Motion correction and PK analysis were performed on all cases. Imaging-derived tumour and non-tumour regions were defined for 14 of 15 lesions (Figure 2). In one case (Patient 006) the heterogeneous mix of tumour components produced wash-in wash-out tumour curves in all subregions defined at initial PCA i.e. it was not possible to define subregions.

Comparison of image-derived and histopathology defined subregions

The DSC for the lesions defined by imaging and histology (Figure 3), and the viable tumour subregions defined by histology and subregion clustering are summarized in Table 1. The lowest DSCs for the $\text{ROI}_{\text{viable}}$ occurred in patient 006, where all tumour subregions, and therefore the entire lesion, were categorized as viable tumour, and for patient 010 and patient 015, which were small lesions with fewer than 200 pixels.

Assessment of viable tumour

The proportion of viable tumour measured by the different methodologies is presented in Table 2. The subregions defined by histopathology and imaging typically overestimated the proportion of viable tumour as defined by histopathological visual assessment. As expected, there was a strong correlation between the proportion of viable tumour defined by subregion cluster between the ROIs and VOIs ($r = 0.934$, $p < 0.001$). Excluding patients where imaging subsegmentation failed (Patient 006), and the lesion resected after chemotherapy (Patient 010), there was a strong correlation between the proportion of viable tumour determined by visual assessment of the histopathology and by imaging ($r = 0.851$, $p < 0.01$).

PK Data Analysis

Comparisons between histopathology-defined and imaging-derived lesion subregions were performed in nine lesions from nine patients. Within-lesion comparisons of imaging-derived subregions within tumour VOIs was performed in 15 lesions in 14 patients, including one lesion in both pre- and post-chemotherapy.

1) There were no significant differences between the K^{trans} or k_{ep} or $T1_0$ values between equivalent imaging-derived and histopathology-defined lesions or viable tumour subregions ($p > 0.1$).
2) There were no significant differences between the K^{trans} or k_{ep} or $T1_0$ values between equivalent 2D ($ROI_{viable\text{-}imaging\text{-}subregion}$) and 3D ($VOI_{viable\text{-}imaging\text{-}subregion}$) subregions ($p > 0.1$).
3) There were significant differences between the K^{trans} and k_{ep} values for the viable tumour and non-viable tumour subregions defined by histopathology ($p < 0.05$): $ROI_{viable\text{-}histopathology\text{-}subregion}$ had significantly higher K^{trans} (0.48 vs 0.28 min^{-1}; $p = 0.039$) and k_{ep} (1.10 vs 0.71 min^{-1}; $p = 0.024$) than $ROI_{nonviable\text{-}histopathology\text{-}subregion}$. There was no difference in $T1_0$ values between viable tumour and non-tumour subregions ($p > 0.1$).
4) There were significant differences between the K^{trans}, k_{ep} and $T1_0$ values for the viable tumour and non-viable tumour subregions defined by imaging ($p < 0.05$): $VOI_{viable\text{-}imaging\text{-}subregion}$ had significantly higher K^{trans} (Figure 4; 0.41 vs 0.21 min^{-1}; $p = 0.001$) and k_{ep} (Figure 5; 1.00 vs 0.58 min^{-1}; $p < 0.001$) and significantly lower $T1_0$ values (1.02 vs 0.89 s, $p < 0.01$) than $VOI_{nonviable\text{-}imaging\text{-}subregion}$.

5) There were significant differences between the K^{trans} and k_{ep} values for the whole lesion and the viable tumour subregions defined by imaging: $VOI_{viable\text{-}imaging\text{-}subregion}$ had significantly higher K^{trans} (Figure 4; 0.41 vs 0.33 min^{-1}; $p < 0.001$) and k_{ep} (Figure 5; 1.00 vs 0.83 min^{-1}; $p<0.001$) than $VOI_{nonviable\text{-}imaging\text{-}subregion}$. There was no difference in $T1_0$ values between viable tumour subregions and the whole lesion ($p=0.1$).

Discussion

This study has used a semi-automated clustering approach based on PCA of DCE-MRI contrast uptake curves to define regions of viable tumour within CRLM. We have demonstrated that distinct subregions can be derived in the majority of patients, and that there is concordance of these subregions with carefully sectioned and coregistered histologically defined subregions.

Pre-defining a region of viable tumour can be used to direct analysis of PK parameter maps. We have demonstrated significant differences between the mean PK parameter values of subregions of viable tumour and non-viable subregions, irrespective of whether these subregions are defined by histopathology or imaging. It is conventional to analyse PK maps by generating and interpreting data for the whole lesion: either deriving a mean contrast-uptake curve, or generating data for each voxel and pooling these data to generate summary statistics.[e.g. 22] Importantly, we have demonstrated that the mean PK data for viable tumour produces significantly different results from the mean PK data for this conventional whole lesion analysis.

Defining a subset of voxels that represent viable tumour has two advantages. Firstly, the voxels represent biologically active tumour and therefore parameters derived from these voxels may correlate more consistently with aspects of tumour biology and outcome. Using DCE-MRI to assess tumour phenotypes has produced mixed results.[23] Non-viable regions, as illustrated in our study, vary significantly from lesion-to-lesion in the proportion of tumour that they represent. If data from both viable and non-viable subregions are incorporated into the summary statistics, these may not consistently reflect properties of the viable tumour. There are some approaches in the literature that have used different methodologies to analyse subsets of PK data, for example based on hot spots[24] or using other data-driven subsets of the parameter maps.[25] Our *a priori* technique defines regions considered to be tumour and then derives PK data for these regions. An advantage of this method is that the extraction of enhancement characteristics and clustering are performed separately on each case based on the variation within the lesion and, therefore, does not require measurement or estimation of the arterial input function, or correction for T10, to perform the segmentation. Other researchers have adopted comparable approaches, for example by defining tumour voxels by the presence of enhancement,[26] or excluding pixels with PK parameter values of zero.[27] However, enhancement is a feature of both viable tumour and other tissues, such as fibrosis, which is a major component of many tumours, including CRLM.[9] We have taken into account the shape of the contrast-uptake curve in defining viable tumour and used a spatially-matched histological gold standard, to confirm voxel-wise concordance of our segmentation methodology.

Secondly, our subregion representation can also been used to quantify viable tumour, which is prognostically relevant,[9] as is the regression of viable tumour in response to chemotherapy.[10] Currently, formal response assessment for CRLM is made using by RECIST 1.1 criteria[7] based on changes in lesion size alone. These do not include any morphological criteria, although it is recognised that morphological changes may improve response characterization.[8] In a small number of patients, our imaging-derived estimates demonstrated a strong correlation with the histopathological assessment of the proportion of viable tumour, for untreated metastases. We did not have a large enough cohort of metastases resected after chemotherapy to assess whether the technique could be useful post-treatment. The ROI-based techniques tended to overestimate the amount of viable tumour compared with visual histological assessment. This is likely to be because the resolution of imaging is lower than microscopic visual assessment, and is insufficient to resolve admixed viable and non-viable tumour components. This was similar to the methodology described by Monsky *et al.*[6] for soft tissue sarcomas, which demonstrated overall correlation, but did not include spatially-matched tumour regions. Our technique could be adapted to generate a composite metric of the volume of viable tumour cells, which may more accurately reflect disease burden and response. Although we have developed this in the setting of resectable liver metastases, in order to allow direct histopathological correlation, this approach could be applied to the larger population of patients with metastatic liver disease who might be treated with palliative chemotherapy or stereotactic internal radiotherapy (SIRT).

One of the limitations of our study is its small sample size. While we were able to show significant differences in PK parameters between tumour subregions. We had insufficient number of patients to assess whether imaging estimates of viable tumour could be used both before and after treatment. This requires further investigation using a larger dataset. Furthermore, the pathological assessments were in two dimensions, as sections were only taken at the central level, rendering it impossible to reconstruct the entire three-dimensional structure of the liver metastases. As a result, the imaging-histopathological correlation analysis could only be performed in 2D.

Another potential limitation is that there were several manual steps in our methodology. Firstly, despite careful sectioning to match the imaging plane, the imaging-histopathology registration involved a manual alignment step to account for fixation and orientation. Secondly, the histopathological subregions were manually defined by experienced observers, rather than automatically defined. During the image analysis, lesions were manually segmented and the subsegmentation strategy involved a supervised stage where automatically generated subregions were merged to create tumour and non-tumour regions. We recognise that fully automated lesion segmentation and tumour subsegmentation would be preferred both to remove variability and to facilitate implementation in the clinical workflow. Automated segmentation of liver lesions is likely to be become routinely available in the future, and is the subject of ongoing investigation, including the evaluation of machine learning techniques[e.g. 28]. The manual component of the subsegmentation process was a very quick step in the software we created, although was a potential source of bias, and future work to allow full automation of this process would be preferred. Machine learning techniques to allow voxel-wise allocation as viable or non-viable tumour based on enhancement characteristics might also be feasible.

In summary, tumour segmentation based on DCE-MRI characteristics can define regions of viable tumour in CRLM. This may have applications for quantitative imaging analysis, and clinical utility as a method of more accurately quantifying tumour burden.

References:

1. Bowel Cancer Statistics. Cancer Research UK Web Site. http://www.cancerresearchuk.org/health-professional/cancer-statistics/statistics-by-cancer-type/bowel-cancer. Accessed August 2016.
2. Howlader N, Noone AM, Krapcho M et al. SEER Cancer Statistics Review, 1975-2013, National Cancer Institute. Bethesda, MD, http://seer.cancer.gov/csr/1975_2013/, based on November 2015 SEER data submission, posted to the SEER web site, April 2016. Accessed August 2016.
3. Hackl C, Neumann P, Gerken M, Loss M, Klinkhammer-Schalke M, Schlitt HJ. Treatment of colorectal liver metastases in Germany: a ten-year population-based analysis of 5772 cases of primary colorectal adenocarcinoma. BMC Cancer. BioMed Central. 2014;14(1):810.
4. Engstrand J, Nilsson H, Strömberg C, Jonas E, Freedman J. Colorectal cancer liver metastases – a population-based study on incidence, management and survival. BMC Cancer. BioMed Central. 2018;18(1):1225–11.
5. Bird NC, Mangnall D, Majeed AW. Biology of colorectal liver metastases: A review. J Surg Oncol. 2006;94(1):68–80.
6. Monsky WL, Jin B, Molloy C, et al. Semi-automated volumetric quantification of tumor necrosis in soft tissue sarcoma using contrast-enhanced MRI. Anticancer Res. 2012;32(11):4951–61.
7. Eisenhauer EA, Therasse P, Bogaerts J, et al. New response evaluation criteria in solid tumours: Revised RECIST guideline (version 1.1). Eur J Cancer. 2009;45(2):228–47.

8. Choi H, Charnsangavej C, Faria SC, et al. Correlation of Computed Tomography and Positron Emission Tomography in Patients With Metastatic Gastrointestinal Stromal Tumor Treated at a Single Institution With Imatinib Mesylate: Proposal of New Computed Tomography Response Criteria. J Clin Oncol. 2007;25(13):1753–9.
9. Maru DM, Kopetz S, Boonsirikamchai P, et al. Tumor thickness at the tumor-normal interface: a novel pathologic indicator of chemotherapy response in hepatic colorectal metastases. Am J Surg Path. 2010;34(9):1287–94.
10. Brouquet A, Zimmitti G, Kopetz S, et al. Multicenter validation study of pathologic response and tumor thickness at the tumor-normal liver interface as independent predictors of disease-free survival after preoperative chemotherapy and surgery for colorectal liver metastases. Cancer. 2013;119(15):2778–88.
11. Viganò L, Capussotti L, De Rosa G, De Saussure WO, Mentha G, Rubbia-Brandt L. Liver resection for colorectal metastases after chemotherapy: impact of chemotherapy-related liver injuries, pathological tumor response, and micrometastases on long-term survival. Ann Surg. 2013;258(5):731–40.
12. Goh V, Padhani AR. Imaging tumor angiogenesis: functional assessment using MDCT or MRI? Abdom Imaging. 2006;31(2):194–9.
13. Zahra MA, Hollingsworth KG, Sala E, Lomas DJ, Tan LT. Dynamic contrast-enhanced MRI as a predictor of tumour response to radiotherapy. Lancet Oncol. 2007;8(1):63–74.
14. Goh V, Halligan S, Gharpuray A, Wellsted D, Sundin J, Bartram CI. Quantitative assessment of colorectal cancer tumor vascular parameters by using perfusion CT: influence of tumor region of interest. Radiology. 2008;247(3):726–32.

15. Irving B, Franklin JM, Papież BW, Anderson EM, Sharma RA, Gleeson FV, et al. Pieces-of-parts for supervoxel segmentation with global context: Application to DCE-MRI tumour delineation. Med Image Anal. 2016;32:69–83.

16. Irving B, Cifor A, Papiez B, et al. Automated colorectal tumour segmentation in DCE-MRI using super-voxel neighbourhood contrast characteristics. MICCAI. 2014;8673:609-16.

17. Kuhl CK, Mielcareck P, Klaschik S, et al. Dynamic breast MR imaging: are signal intensity time course data useful for differential diagnosis of enhancing lesions? Radiology. 1999;211(1):101–10.

18. Kimura T, Hirokawa Y, Murakami Y, Tsujimura M, Nakashima T, Ohno Y, et al. Reproducibility of organ position using voluntary breath-hold method with spirometer for extracranial stereotactic radiotherapy. Int J Radiat Oncol Biol Phys. 2004 Nov 15;60(4):1307–13.

19. Papież BW, Franklin JM, Heinrich MP, Gleeson FV, Schnabel JA. Liver Motion Estimation via Locally Adaptive Over-Segmentation Regularization. MICCAI. 2015;9351:427–434.

20. Orton MR, Miyazaki K, Koh D-M, et al. Optimizing functional parameter accuracy for breath-hold DCE-MRI of liver tumours. Phys Med Biol. 2009;54(7):2197–215.

21. Dice, Lee R. (1945). Measures of the Amount of Ecologic Association Between Species. Ecology. 26 (3):297–302.

22. Morgan B, Utting JF, Higginson A, Thomas AL, Steward WP, Horsfield MA. A simple, reproducible method for monitoring the treatment of tumours using dynamic contrast-enhanced MR imaging. Br J Cancer. 2006;94:1420–7.

23. O'Connor JPB, Jackson A, Parker GJM, Jayson GC. DCE-MRI biomarkers in the clinical evaluation of antiangiogenic and vascular disrupting agents. Br J Cancer. 2007;96(2):189–95.

24. Jackson A, O'Connor JPB, Parker GJM, Jayson GC. Imaging tumor vascular heterogeneity and angiogenesis using dynamic contrast-enhanced magnetic resonance imaging. Clin Cancer Res. 2007 Jun 15;13(12):3449–59.

25. Hayes C, Padhani AR, Leach MO. Assessing changes in tumour vascular function using dynamic contrast-enhanced magnetic resonance imaging. NMR Biomed. 2002;15(2):154–63.

26. de Lussanet QG, Backes WH, Griffioen AW, et al. Dynamic contrast-enhanced magnetic resonance imaging of radiation therapy-induced microcirculation changes in rectal cancer. Int J Radiat Oncol Biol Phys. 2005;63(5):1309–15.

27. O'Connor JPB, Rose CJ, Jackson A, et al. DCE-MRI biomarkers of tumour heterogeneity predict CRC liver metastasis shrinkage following bevacizumab and FOLFOX-6. Br J Cancer. 2011;105(1):139–45.

28. Chlebus G, Schenk A, Moltz JH, van Ginneken B, Hahn HK, Meine H. Automatic liver tumor segmentation in CT with fully convolutional neural networks and object-based postprocessing. Scientific Reports. 2018;19;8(1):15497.

Legends to Tables

Table 1:

Dice similarity coefficients comparing $\mathrm{ROI}_{\text{lesion-histopathology}}$ with $\mathrm{ROI}_{\text{lesion-imaging,}}$ and comparing $\mathrm{ROI}_{\text{viable-imaging-subregion}}$ with $\mathrm{ROI}_{\text{viable-histopathology}}$

Table 2:

Proportion of viable tumour (%) by visual assessment of the histopathology, and calculated from the histopathology-defined and imaging-derived subregions.

Legends to Figures

Figure 1:

Image 1a is H&E stained histopathology slide of a 30mm resected colorectal liver metastasis demonstrating peripheral viable tumour with a centrally necrotic region. In image B the $\mathrm{ROI}_{\text{lesion-histopathology}}$ is outlined (black line) and the regions $\mathrm{ROI}_{\text{viable-histopathology}}$ (solid grey region) and $\mathrm{ROI}_{\text{nonviable-histopathology}}$ (shaded grey region) are shown.

Figure 2:

Two-stage semi-automated segmentation of manually delineated liver metastasis by PCA clustering based on DCE-MRI signal-time curves. Image 2a and 2c show the four automatically defined subregions within $\mathrm{VOI}_{\text{lesion-imaging}}$ and images 2b and 2d show the four mean signal-time curves for the equivalent regions. The three wash-in wash-out curves (Image 2b, labels 1, 2 and 4) were merged to create $\mathrm{VOI}_{\text{viable-imaging-subregion}}$ while the remaining voxels are classified as $\mathrm{VOI}_{\text{nonviable-imaging-subregion}}$.

Figure 3:

Image 3a shows the spatial overlap of $\mathrm{ROI}_{\text{lesion-histopathology}}$ (green outline) and $\mathrm{ROI}_{\text{lesion-imaging}}$ (red outline). Image 3b shows the spatial overlap of $\mathrm{ROI}_{\text{viable-histopathology}}$ (between outer green outline and inner red outline) and $\mathrm{ROI}_{\text{viable-imaging-subregion}}$ (between outer green and inner green outline; derived from $\mathrm{ROI}_{\text{lesion-histopathology}}$). Dice similarity coefficients were 0.834 and 0.93, respectively.

Figure 4:

Mean K^{trans} of colorectal liver metastases (dark blue) image VOIs and of image-derived tumour (purple) and non-tumour subregions (green).

Figure 5:

Mean k_{ep} of colorectal liver metastases (dark blue) image VOIs and of image-derived tumour (purple) and non-tumour subregions (green).

Figure 6:

Image 6a is a resected colorectal liver metastasis with central non-viable tumour (NV) and a rim of viable (V) tumour. Image 6b is the K^{trans} map for the whole lesion and Image 6b is the K^{trans} map for the viable tumour subregion only.

Tumour subregion analysis of colorectal liver metastases using semi-automated clustering based on DCE-MRI: comparison with histological subregions and impact on pharmacokinetic parameter analysis

Abstract

Purpose

To use a novel segmentation methodology based on dynamic contrast-enhanced magnetic resonance imaging (DCE-MRI) to define tumour subregions of liver metastases from colorectal cancer (CRC), to compare these with histology, and to use these to compare extracted pharmacokinetic (PK) parameters between tumour subregions.

Materials and Methods

This ethically-approved prospective study recruited patients with CRC and ≥1 hepatic metastases scheduled for hepatic resection. Patients underwent DCE-MRI pre-metastasectomy. Histological sections of resection specimens were spatially matched to DCE-MRI acquisitions and used to define histological subregions of viable and non-viable tumour. A semi-automated voxel-wise image segmentation algorithm based on the DCE-MRI contrast-uptake curves was used to define imaging subregions of viable and non-viable tumour. Overlap of histologically-defined and imaging subregions was compared using the Dice similarity coefficient (DSC). DCE-MRI PK parameters were compared for the whole tumour and histology-defined and imaging-derived subregions.

Results:

Fourteen patients were included in the analysis. Direct histological comparison with imaging was possible in nine patients. Mean DSC for viable tumour subregions defined by imaging and histology was 0.738 (range 0.540-0.930). There were significant differences between K^{trans} and k_{ep} for viable and non-viable subregions ($p<0.001$) and between whole lesions and viable subregions ($p<0.001$).

Conclusion:

We demonstrate good concordance of viable tumour segmentation based on preoperative DCE-MRI with a post-operative histological gold-standard. This can be used to extract viable tumour-specific values from quantitative image analysis, and could improve treatment response assessment in clinical practice.

Keywords

Liver Neoplasm;

Colorectal Neoplasm;

MRI;

Perfusion Imaging.

Abbreviations

CRC – colorectal cancer

CRLM – colorectal liver metastases

DCE-MRI – dynamic contrast enhanced MRI

IB – imaging biomarkers

PK – pharmacokinetic

RECIST – response evaluation criteria in solid tumours

ROI – region of interest

VOI – volume of interest

Introduction

Colorectal cancer (CRC) is the fourth most common cancer in the UK[1] and US[2]. Colorectal liver metastases (CRLM) complicate approximately 25% of cases of CRC, either at the time of presentation or during follow-up.[3,4] CRLM are pathologically heterogeneous, comprising regions of viable, cellular tumour as well as areas of predominantly acellular fibrosis and necrosis. For patients with CRC, primary and metastatic lesions may also contain mucinous regions and areas of calcification.[5]

Cellular regions of tumour have different MRI characteristics from other components,[6] and could be used as the basis for tumour subsegmentation. Segmenting viable tumour regions using *in vivo* imaging could have substantial clinical utility. Firstly, it may assist in assessing response to treatment: conventional size-based response criteria such as RECIST 1.1[7] assume that all treatment response is associated with changes in tumour size; incorporating morphological response criteria can improve response assessment in some settings.[8] Secondly, in patients with CRLM, pathological assessment of viable tumour[9,10] and the composition of the metastasis[11] are prognostically relevant. However, there is no reliable methodology to quantify this *in vivo*, where it could be used to influence clinical decision-making.

Segmentation of viable tumour regions by imaging also has the potential to improve analysis of quantitative imaging data. Extraction of quantitative imaging biomarkers (IB) has typically been based on analysis of the whole lesion, which includes acellular regions, as well as the regions of viable tumour. When analysing pharmacokinetic (PK) data derived from, for example, dynamic contrast-enhanced MRI (DCE-MRI), it may be preferable to focus on regions of viable tumour. This could improve on the variable associations found between perfusion imaging and histological parameters observed to date,[12,13] and improve tumour phenotyping by imaging. Finally, manual delineation of tumour subregions for pharmacokinetic (PK) analysis introduces intra-observer variability,[14,15] and may be impractical in clinical practice, and therefore automated or semi-automated segmentation is preferred.

We developed a methodology to semi-automatically segment tumour and non-tumour regions based on DCE-MRI characteristics. This study has two aims: firstly, to compare these subregions with a reference standard of histological subregions from spatially matched resected CRLM and, secondly, to analyse the impact of using these tumour subregions to examine DCE-MRI-derived PK data.

Methods and Materials

Patients

Patients were eligible for this ethically approved prospective observational study if they had a diagnosis of CRC, at least one hepatic metastasis ≥8mm not previously treated with systematic chemotherapy and were scheduled for surgical liver metastasectomy. All patients provided written informed consent to the study procedures. DCE-MRI of the liver was performed at baseline and then patients either proceeded directly to surgery, or were treated with neoadjuvant chemotherapy as part of their routine clinical care. To minimise changes to tumour morphology between pre-operative imaging and histopathological assessment, patients were excluded from the imaging-histopathology correlation analysis if the interval between DCE-MRI and surgery exceeded 28 days.

DCE-MRI technique

MRI studies were performed at 1.5T (GE HDX Twinspeed MR scanner; GE, Milkwaukee, WI) with an 8-channel torso coil. All DCE-MRI imaging was performed in the axial plane. A multiparametric MRI incorporating T2 weighted (T2W), T1 weighted (T1W), diffusion weighted (DWI) and DCE-MRI was performed. DCE-MRI was performed using multiple flip-angle (15°,9° and 3°) sequences to calculate voxel $T1_0$ values followed by T1W imaging (axial 3D multiphase LAVA (imaging options: Fast, ZIP2 Asset), acceleration factor = 1.00, ~~;~~field of view = 42, phase FOV = 0.8, matrix 320 x 192, slice thickness = 5.0 mm, pixel size = 1.31 x 1.75 x 5 mm, location per slab = 22, overlap = 0, TR = 4.46 s, TE = 2.128 s) of a predefined volume centered on the largest liver metastasis before and after the injection of a 15 mL bolus of gadolinium chelate (Gadoteridol; ProHance, Bracco Diagnostics, Princeton, USA), with a 15 mL saline flush. Volumes were acquired over a 7s breath-hold during end-expiration for at least 7 minutes after contrast administration, with lengthening interscan intervals (0-2 minutes – 1 breath cycle between each acquisition; 2-4 minutes: 2 breath cycles between each acquisition; 4-6 minutes: 3 breath cycles between each acquisition; 6+ minutes: 4 breath cycles between each acquisition). All studies had at least 20 acquisitions to inform the PK-modelling.

Histopathological cut-up and staining

At the time of hepatic resection the specimen was oriented perpendicular to the craniocaudal axis and the anterior surface marked. The midpoint of the metastasis in the craniocaudal axis was identified using *ex-vivo* ultrasound and marked superficially on the specimen. For deep lesions, an ultrasound examination was performed at the time of histological cut-up.

Histopathological cut-up was performed prior to formalin fixation. Liver specimens were sectioned in the axial plane at the meridian of the selected metastasis based on the surgical and sonographic landmarks, with further approximately five millimeter sections taken through the metastasis. The sections were marked (anterior, posterior, medial and lateral), photographed, and then transferred to cassettes. Sections were fixed overnight in formalin and embedded in paraffin. Three micrometer sections of each metastasis at the midpoint section were cut and stained using haematoxylin and eosin (H&E), and mounted on glass slides.

Histopathological analysis

H&E stained slides were reviewed, using light microscopy, jointly by two consultant histopathologists with >10 years experience in reporting CRC histopathology. Each metastasis was scored by consensus, blinded to all clinical and imaging data, for the percentage of four principal components of CRLM: viable tumour, fibrosis, necrosis and mucin to the nearest 5%. This was used to determine proportion of viable tumour estimate by visual assessment.

Image-histopathology alignment

Histopathology slides were scanned digitally (Aperio CS2 Slidescanner, Leica Biosystems, USA) and imported into OsiriX 2 DICOM Viewer (Pixmeo SARL, Bernex, Switzerland) as converted DICOM files (JPEG to DICOM v2.0). DCE-MRI studies were also imported. Histopathological images were scaled to match the tumour on MRI to allow for size reduction during formalin fixation: the entire lesion was manually measured in the longest axial plane (x-dimension) and in the longest perpendicular (y-dimension) at both imaging and histopathology. The histopathology images were then rescaled to match the x- and y-dimensions of the lesion on MRI.

Histopathological images were fused with the DCE-MRI 4D volume and manually aligned to match the lesion contour in the imaging space, based on the histopathological orientation and local features such as the liver capsule or local blood vessels.

Lesion subregion derivation

The entire metastatic lesion ($\mathrm{ROI}_{\text{lesion-histopathology}}$) and the subregion(s) of viable tumour ($\mathrm{ROI}_{\text{viable-histopathology}}$) were manually delineated on the histopathology image, and saved in the imaging space (Figure 1). $\mathrm{ROI}_{\text{viable-histopathology}}$ encompassed regions of predominantly viable, cellular tumour. Non-contiguous tumour regions less than 500 µm in diameter were not included. To derive the non-viable tumour ROI ($\mathrm{ROI}_{\text{non-viable-histopathology}}$), the $\mathrm{ROI}_{\text{viable-histopathology}}$ was subtracted from $\mathrm{ROI}_{\text{lesion-histopathology}}$.

The whole volume of the metastatic lesion ($\mathrm{VOI}_{\text{lesion-imaging}}$) was manually delineated on the unenhanced T1W images, or, in cases where the lesion was better defined or larger, using the T2W images, by a radiologist with seven ~~years experience~~years’ experience reporting liver MRI.

The imaging subregion analysis was performed using in-house software. To create the image-derived subregions the contrast uptake curves for the voxels within $\mathrm{VOI}_{\text{lesion-imaging}}$ and $\mathrm{ROI}_{\text{lesion-histopathology}}$ were analysed using a principal component analysis (PCA) of the DCE-MRI enhancement curves, followed by k-means clustering of these modes, as described in a prior publication.[16] Based on a retrospective analysis of the dataset, t~~T~~hree PCA modes were found to capture the variation in the data, and best separate regions of different contrast uptake characteristics, and were used to automatically define four subregions. These four subregions were subsequently manually merged into two regions: viable tumour, identified by a wash-in/wash-out curve, and non-viable tumour, where there were other contrast curves (non-enhancing or contrast accumulation; Figure 2) as described by Kuhl *et al*.[17]

Thus for the VOI$_{\text{lesion-imaging}}$ two regions were defined: VOI$_{\text{viable-imaging-subregion}}$ and VOI$_{\text{nonviable-imaging-subregion}}$. Two regions were also defined within ROI$_{\text{lesion-histopathology}}$: ROI$_{\text{viable-imaging-subregion}}$ and ROI$_{\text{nonviable-imaging-subregion}}$.

DCE-MRI analysis

There were three stages to derivation of the PK parameters from DCE-MRI:

i. Motion correction

The liver is subject to respiratory motion. Although images were acquired in end expiration, which minimizes inter-frame motion (Kimura *et al*, 2004[18]), there was residual inter-frame motion. This was corrected using a non-rigid motion correction algorithm developed using liver DCE-MRI studies as we have previously described, which results in significant improvement in the registration error.[19~~8~~]

ii. PK analysis

The variable flip angle sequence was registered to the baseline image of the DCE-MRI image and used to derive baseline T1 values ($T1_0$) and, for each voxel in the DCE-MRI acquisition, signal was converted to contrast concentration. The Toft’s model, using population-average portal venous and arterial input functions[20~~19~~], was fitted to the contrast enhancement curve of each voxel to produce maps of PK parameters.

iii. Extraction of PK parameters

The PK parameter maps were imported into proprietary in-house PK View software, which was developed to aid this analysis.[16] Mean, median, deviation, minimum and maximum values for K^{trans}, k_{ep} and $T1_0$ for each of the defined ROIs and VOIs were derived.

Data Analysis

i. Comparison of image-derived and histopathology defined subregions

To assess the agreement between regions defined on ~~‘gold standard’~~ histopathology with those semi-automatically determined from imaging, the spatial overlaps of $\text{ROI}_{\text{lesion-imaging}}$ and $\text{ROI}_{\text{lesion-histopathology}}$, and $\text{ROI}_{\text{viable-imaging-subregion}}$ and $\text{ROI}_{\text{viable-histopathology}}$ were estimated using the Dice similarity coefficient (DSC)[21~~0~~], as shown in Figure 3).

ii. Assessment of viable tumour

The percentage of viable tumour for the whole histopathology slide was reported by visual assessment by agreement of two consultant histopathologists. The percentage of viable tumour within the histopathology ROI and imaging ROI and VOI image were calculated:

- Histopathology: $100 * \text{ROI}_{\text{viable-histopathology}}/\text{ROI}_{\text{lesion-histopathology}}$
- ROI imaging $100 * \text{ROI}_{\text{viable-imaging}}/\text{ROI}_{\text{lesion-imaging}}$
- VOI imaging $100 * \text{VOI}_{\text{viable-imaging}}/\text{VOI}_{\text{lesion-imaging}}$

These values were correlated using the Pearson product-moment correlation coefficient.

iii. PK data analysis

$T1_0$ and PK parameters were summarized for each of the ROI/VOIs and presented graphically. The following $T1_0$ PK parameters comparisons were performed using paired Student's T-test. p-values of <0.05 were taken to be significant.

To compare viable tumour subregions defined by imaging and defined by histopathology:

1) $ROI_{viable\text{-}imaging\text{-}subregion}$ and $ROI_{viable\text{-}histopathology}$

To compare viable tumour subregions defined by imaging in 2D and in 3D:

2) $ROI_{viable\text{-}imaging\text{-}subregion}$ and $VOI_{viable\text{-}imaging\text{-}subregion}$

To compare viable and non-viable subregions:

3) $ROI_{viable\text{-}histopathology}$ and $ROI_{nonviable\text{-}histopathology}$
4) $VOI_{viable\text{-}imaging\text{-}subregion}$ and $VOI_{nonviable\text{-}imaging\text{-}subregion}$

To compare the whole lesion with only the viable component:

5) $VOI_{lesion\text{-}imaging\text{-}subregion}$ and $VOI_{viable\text{-}imaging\text{-}subregion}$

Results

Patients

Fifteen patients were recruited to this prospective study. One patient was withdrawn. The remaining fourteen underwent hepatic metastasectomy. Of these fourteen patients, ten patients proceeded directly to metasectomy and four patients were treated with neoadjuvant chemotherapy. One patient declined post-treatment DCE-MRI, otherwise DCE-MRI was performed successfully in all cases at baseline and after chemotherapy where appropriate; and this provided the study dataset. Direct histological comparison with imaging was possible in nine patients: eight patients not treated with neoadjuvant chemotherapy and in one patient (patient 010) treated with neoadjuvant chemotherapy. One patient declined post-treatment DCE-MRI, one had further chemotherapy after post-treatment DCE-MRI, the specimen was not available for one patient, and one patient treated with chemotherapy had a complete pathological response at the time of resection, precluding direct assessment of imaging and histology. In one patient there was recurrence at a prior resection margin, with multiple small tumour islands, which it was not possible to co-register reliably with the DCE-MRI images.

Histopathology analysis

Viable tumour and non-viable subregions were defined for all patients as described above (see Figure 1).

Image analysis

Motion correction and PK analysis were performed on all cases. Imaging-derived tumour and non-tumour regions were defined for 14 of 15 lesions (Figure 2). In one case (Patient 006) the heterogeneous mix of tumour components produced wash-in wash-out tumour curves in all subregions defined at initial PCA i.e. it was not possible to define subregions.

Comparison of image-derived and histopathology defined subregions

The DSC for the lesions defined by imaging and histology (Figure 3), and the viable tumour subregions defined by histology and subregion clustering are summarized in Table 1~~2~~. The lowest DSCs for the $\mathrm{ROI}_{\mathrm{viable}}$ occurred in patient 006, where all tumour subregions, and therefore the entire lesion, were categorized as viable tumour, and for patient 010 and patient 015, which were small lesions with fewer than 200 pixels.

Assessment of viable tumour

The proportion of viable tumour measured by the different methodologies is presented in Table 2. The subregions defined by histopathology and imaging typically overestimated the proportion of viable tumour as defined by histopathological visual assessment. As expected, there was a strong correlation between the proportion of viable tumour defined by subregion cluster between the ROIs and VOIs ($r = 0.934$, $p < 0.001$). Excluding patients where imaging subsegmentation failed (Patient 006), and the lesion resected after chemotherapy (Patient 010), there was a strong correlation between the proportion of viable tumour determined by visual ~~interpretation~~ assessment of the histopathology and by imaging ($r = 0.851$, $p < 0.01$).

PK Data Analysis

Comparisons between histopathology-defined and imaging-derived lesion subregions were performed in nine lesions from nine patients. Within-lesion comparisons of imaging-derived subregions within tumour VOIs was performed in 15 lesions in 14 patients, including one lesion in both pre- and post-chemotherapy.

1) There were no significant differences between the K^{trans} or k_{ep} or $T1_0$ values between equivalent imaging-derived and histopathology-defined lesions or viable tumour subregions ($p > 0.1$).
2) There were no significant differences between the K^{trans} or k_{ep} or $T1_0$ values between equivalent 2D ($ROI_{viable\text{-}imaging\text{-}subregion}$) and 3D ($VOI_{viable\text{-}imaging\text{-}subregion}$) subregions ($p > 0.1$).
3) There were significant differences between the K^{trans} and k_{ep} values for the viable tumour and non-viable tumour subregions defined by histopathology ($p < 0.05$): $ROI_{viable\text{-}histopathology\text{-}subregion}$ had significantly higher K^{trans} (0.48 vs 0.28 min^{-1}; $p = 0.039$) and k_{ep} (1.10 vs 0.71 min^{-1}; $p = 0.024$) than $ROI_{nonviable\text{-}histopathology\text{-}subregion}$. There was no difference in $T1_0$ values between viable tumour and non-tumour subregions ($p > 0.1$).

4) There were significant differences between the K^{trans}, k_{ep} and $T1_0$ values for the viable tumour and non-viable tumour subregions defined by imaging ($p < 0.05$): $VOI_{viable\text{-}imaging\text{-}subregion}$ had significantly higher K^{trans} (Figure 4; 0.41 vs 0.21~~2~~ min^{-1}; p =~~<~~ 0.001) and k_{ep} (Figure 5; 1.00 vs 0.~~63~~ 58 min^{-1}; $p < 0.001$) and significantly lower $T1_0$ values (1.02~~3~~ vs 0.89 s, p <~~=~~ 0.01) than $VOI_{nonviable\text{-}imaging\text{-}subregion}$.

5) There were significant differences between the K^{trans} and k_{ep} values for the whole lesion and the viable tumour subregions defined by imaging: $VOI_{viable\text{-}imaging\text{-}subregion}$ had significantly higher K^{trans} (Figure 4; 0.41 vs 0.33 min^{-1}; $p < 0.001$) and k_{ep} (Figure 5; 1.00 vs 0.83 min^{-1}; $p<0.001$) than $VOI_{nonviable\text{-}imaging\text{-}subregion}$. There was no difference in $T1_0$ values between viable tumour subregions and the whole lesion ($p=0.1$).

Discussion

This study has used a semi-automated clustering approach based on PCA of DCE-MRI contrast uptake curves to define regions of viable tumour within CRLM. We have demonstrated that distinct subregions can be derived in the majority of patients, and that there is concordance of these subregions with carefully sectioned and coregistered histologically defined subregions.

Pre-defining a region of viable tumour can be used to direct analysis of PK parameter maps. We have demonstrated significant differences between the mean PK parameter values of subregions of viable tumour and non-viable subregions, irrespective of whether these subregions are defined by histopathology or imaging. It is conventional to analyse PK maps by generating and interpreting data for the whole lesion: either deriving a mean contrast-uptake curve, or generating data for each voxel and pooling these data to generate summary statistics.~~[22]~~[e.g. 22] Importantly, we have demonstrated that the mean PK data for viable tumour produces significantly different results from the mean PK data for this conventional whole lesion analysis.

Defining a subset of voxels that represent viable tumour has two advantages. Firstly, the voxels represent biologically active tumour and therefore parameters derived from these voxels may correlate more consistently with aspects of tumour biology and outcome. Using DCE-MRI to assess tumour phenotypes has produced mixed results.~~[22]~~[23] Non-viable regions, as illustrated in our study, vary significantly from lesion-to-lesion in the proportion of tumour that they represent. If data from both viable and non-viable subregions are incorporated into the summary statistics, these may not consistently reflect properties of the viable tumour. There are some approaches in the literature that have used different methodologies to analyse subsets of PK data, for example based on hot ~~spots[23]~~ spots[24] or using other data-driven subsets of the parameter maps.[25]~~[24]~~ Our *a priori* technique defines regions considered to be tumour and then derives PK data for these regions. An advantage of this method is that the extraction of enhancement characteristics and clustering are performed separately on each case based on the variation within the lesion and, therefore, does not require measurement or estimation of the arterial input function, or correction for T10, to perform the segmentation. Other researchers have adopted comparable approaches, for example by defining tumour voxels by the presence of enhancement,[26]~~[25]~~ or excluding pixels with PK parameter values of zero.[~~2~~27~~6~~] However, enhancement is a feature of both viable tumour and other tissues, such as fibrosis, which is a major component of many tumours, including CRLM.[9] We have taken into account the shape of the contrast-uptake curve in defining viable tumour and used a spatially-matched histological gold standard, to confirm voxel-wise concordance of our segmentation methodology.

Secondly, our subregion representation can also been used to quantify viable tumour, which is prognostically relevant,[9] as is the regression of viable tumour in response to chemotherapy.[10] Currently, formal response assessment for CRLM is made using by RECIST 1.1 criteria[7] based on changes in lesion size alone. These do not include any morphological criteria, although it is recognised that morphological changes may improve response characterization.[8] In a small number of patients, our imaging-derived estimates demonstrated a strong correlation with the histopathological assessment of the proportion of viable tumour, for untreated metastases. We did not have a large enough cohort of metastases resected after chemotherapy to assess whether the technique could be useful post-treatment. The ROI-based techniques tended to overestimate the amount of viable tumour compared with visual histological assessment. This is likely to be because the resolution of imaging is lower than microscopic visual assessment, and is insufficient to resolve admixed viable and non-viable tumour components. This was similar to the methodology described by Monsky *et al*.[6] for soft tissue sarcomas, which demonstrated overall correlation, but did not include spatially-matched tumour regions. Our technique could be adapted to generate a composite metric of the volume of viable tumour cells, which may more accurately reflect disease burden and response. Although we have developed this in the setting of resectable liver metastases, in order to allow direct histopathological correlation, this approach could be applied to the larger population of patients with metastatic liver disease who might be treated with palliative chemotherapy or stereotactic internal radiotherapy (SIRT).

One of the limitations of our study is its small sample size. While we were able to show significant differences in PK parameters between tumour subregions. We had insufficient number of patients to assess whether imaging estimates of viable tumour could be used both before and after treatment. This requires further investigation using a larger dataset. Furthermore, the pathological assessments were in two dimensions, as sections were only taken at the central level, rendering it impossible to reconstruct the entire three-dimensional structure of the liver metastases. As a result, the imaging-histopathological correlation analysis could only be performed in 2D.

~~There~~ Another potential limitation is that there were ~~also~~ several manual steps in our methodology. Firstly, despite careful sectioning to match the imaging plane, the imaging-histopathology registration involved a manual alignment step to account for fixation and orientation. Secondly, the histopathological subregions were manually defined by experienced observers, rather than automatically defined. During the image analysis, lesions were manually segmented and the ~~Finally, our~~sub~~-~~segmentation strategy involved a supervised stage where automatically generated subregions were merged to create tumour and non-tumour regions. We recognise that ~~a~~ fully automated lesion segmentation and tumour subsegmentation would be preferred both to remove variability and to facilitate implementation in the clinical workflow. Automated segmentation of liver lesions is likely to be become routinely available in the future, and is the subject of ongoing investigation, including the evaluation of machine learning techniques[e.g. 28]. The manual component of the subsegmentation process was a very quick step in the software we created, although was a potential

Formatted: Superscript

source of bias, and future work to allow full automation of this process would be preferred. Machine learning techniques to allow voxel-wise allocation as viable or non-viable tumour based on enhancement characteristics might also be feasible.

In summary, tumour segmentation based on DCE-MRI characteristics can define regions of viable tumour in CRLM. This may have applications for quantitative imaging analysis, and clinical utility as a method of more accurately quantifying tumour burden.

References:

1. Bowel Cancer Statistics. Cancer Research UK Web Site. http://www.cancerresearchuk.org/health-professional/cancer-statistics/statistics-by-cancer-type/bowel-cancer. Accessed August 2016.
2. Howlader N, Noone AM, Krapcho M et al. SEER Cancer Statistics Review, 1975-2013, National Cancer Institute. Bethesda, MD, http://seer.cancer.gov/csr/1975_2013/, based on November 2015 SEER data submission, posted to the SEER web site, April 2016. Accessed August 2016.

3. Hackl C, Neumann P, Gerken M, Loss M, Klinkhammer-Schalke M, Schlitt HJ. Treatment of colorectal liver metastases in Germany: a ten-year population-based analysis of 5772 cases of primary colorectal adenocarcinoma. BMC Cancer. BioMed Central. 2014;14(1):810.

4. Engstrand J, Nilsson H, Strömberg C, Jonas E, Freedman J. Colorectal cancer liver metastases – a population-based study on incidence, management and survival. BMC Cancer. BioMed Central. 2018;18(1):1225–11.

5. Bird NC, Mangnall D, Majeed AW. Biology of colorectal liver metastases: A review. J Surg Oncol. 2006;94(1):68–80.
6. Monsky WL, Jin B, Molloy C, et al. Semi-automated volumetric quantification of tumor necrosis in soft tissue sarcoma using contrast-enhanced MRI. Anticancer Res. 2012;32(11):4951–61.
7. Eisenhauer EA, Therasse P, Bogaerts J, et al. New response evaluation criteria in solid tumours: Revised RECIST guideline (version 1.1). Eur J Cancer. 2009;45(2):228–47.
8. Choi H, Charnsangavej C, Faria SC, et al. Correlation of Computed Tomography and Positron Emission Tomography in Patients With Metastatic Gastrointestinal Stromal Tumor Treated at a Single Institution With Imatinib Mesylate: Proposal of New Computed Tomography Response Criteria. J Clin Oncol. 2007;25(13):1753–9.
9. Maru DM, Kopetz S, Boonsirikamchai P, et al. Tumor thickness at the tumor-normal interface: a novel pathologic indicator of chemotherapy response in hepatic colorectal metastases. Am J Surg Path. 2010;34(9):1287–94.

10. Brouquet A, Zimmitti G, Kopetz S, et al. Multicenter validation study of pathologic response and tumor thickness at the tumor-normal liver interface as independent predictors of disease-free survival after preoperative chemotherapy and surgery for colorectal liver metastases. Cancer. 2013;119(15):2778–88.
11. Viganò L, Capussotti L, De Rosa G, De Saussure WO, Mentha G, Rubbia-Brandt L. Liver resection for colorectal metastases after chemotherapy: impact of chemotherapy-related liver injuries, pathological tumor response, and micrometastases on long-term survival. Ann Surg. 2013;258(5):731–40.
12. Goh V, Padhani AR. Imaging tumor angiogenesis: functional assessment using MDCT or MRI? Abdom Imaging. 2006;31(2):194–9.
13. Zahra MA, Hollingsworth KG, Sala E, Lomas DJ, Tan LT. Dynamic contrast-enhanced MRI as a predictor of tumour response to radiotherapy. Lancet Oncol. 2007;8(1):63–74.
14. Goh V, Halligan S, Gharpuray A, Wellsted D, Sundin J, Bartram CI. Quantitative assessment of colorectal cancer tumor vascular parameters by using perfusion CT: influence of tumor region of interest. Radiology. 2008;247(3):726–32.
15. Irving B, Franklin JM, Papież BW, Anderson EM, Sharma RA, Gleeson FV, et al. Pieces-of-parts for supervoxel segmentation with global context: Application to DCE-MRI tumour delineation. Med Image Anal. 2016;32:69–83.
16. Irving B, Cifor A, Papiez B, et al. Automated colorectal tumour segmentation in DCE-MRI using super-voxel neighbourhood contrast characteristics. MICCAI. 2014;8673:609-16.

17. Kuhl CK, Mielcareck P, Klaschik S, et al. Dynamic breast MR imaging: are signal intensity time course data useful for differential diagnosis of enhancing lesions? Radiology. 1999;211(1):101–10.

18. Kimura T, Hirokawa Y, Murakami Y, Tsujimura M, Nakashima T, Ohno Y, et al. Reproducibility of organ position using voluntary breath-hold method with spirometer for extracranial stereotactic radiotherapy. Int J Radiat Oncol Biol Phys. 2004 Nov 15;60(4):1307–13.

~~18.~~19. Papież BW, Franklin JM, Heinrich MP, Gleeson FV, Schnabel JA. Liver Motion Estimation via Locally Adaptive Over-Segmentation Regularization. MICCAI. 2015;9351:427–434.

~~19.~~20. Orton MR, Miyazaki K, Koh D-M, et al. Optimizing functional parameter accuracy for breath-hold DCE-MRI of liver tumours. Phys Med Biol. 2009;54(7):2197–215.

~~20.~~21. Dice, Lee R. (1945). Measures of the Amount of Ecologic Association Between Species. Ecology. 26 (3):297–302.

~~21.~~22. Morgan B, Utting JF, Higginson A, Thomas AL, Steward WP, Horsfield MA. A simple, reproducible method for monitoring the treatment of tumours using dynamic contrast-enhanced MR imaging. Br J Cancer. 2006;94:1420–7.

~~22.~~23. O'Connor JPB, Jackson A, Parker GJM, Jayson GC. DCE-MRI biomarkers in the clinical evaluation of antiangiogenic and vascular disrupting agents. Br J Cancer. 2007;96(2):189–95.

~~23.~~24. Jackson A, O'Connor JPB, Parker GJM, Jayson GC. Imaging tumor vascular heterogeneity and angiogenesis using dynamic contrast-enhanced magnetic resonance imaging. Clin Cancer Res. 2007 Jun 15;13(12):3449–59.

Formatted: Font: Calibri, 12 pt

Formatted: Line spacing: Double

~~24.~~25. Hayes C, Padhani AR, Leach MO. Assessing changes in tumour vascular function using dynamic contrast-enhanced magnetic resonance imaging. NMR Biomed. 2002;15(2):154–63.

~~25.~~26. de Lussanet QG, Backes WH, Griffioen AW, et al. Dynamic contrast-enhanced magnetic resonance imaging of radiation therapy-induced microcirculation changes in rectal cancer. Int J Radiat Oncol Biol Phys. 2005;63(5):1309–15.

O'Connor JPB, Rose CJ, Jackson A, et al. DCE-MRI biomarkers of tumour heterogeneity predict CRC liver metastasis shrinkage following bevacizumab and FOLFOX-6. Br J Cancer. 2011;105(1):139–45.

27.

28. Chlebus G, Schenk A, Moltz JH, van Ginneken B, Hahn HK, Meine H. Automatic liver tumor segmentation in CT with fully convolutional neural networks and object-based postprocessing. Scientific Reports. 2018;19;8(1):15497.

Formatted: List Paragraph, Line spacing: Double, Numbered + Level: 1 + Numbering Style: 1, 2, 3, … + Start at: 1 + Alignment: Left + Aligned at: 0" + Indent at: 0.3"

Formatted: Font: Calibri

Formatted: Font: Calibri

Formatted: List Paragraph, Line spacing: Double, Numbered + Level: 1 + Numbering Style: 1, 2, 3, … + Start at: 1 + Alignment: Left + Aligned at: 0" + Indent at: 0.3"

Legends to Tables

Table 1:

Dice similarity coefficients comparing $\mathrm{ROI}_{\text{lesion-histopathology}}$ with $\mathrm{ROI}_{\text{lesion-imaging,}}$ and comparing $\mathrm{ROI}_{\text{viable-imaging-subregion}}$ with $\mathrm{ROI}_{\text{viable-histopathology}}$

Table 2:

Proportion of viable tumour (%) by visual assessment of the histopathology, and calculated from the histopathology-defined and imaging-derived subregions.

Legends to Figures

Figure 1:

Image 1a is H&E stained histopathology slide of a 30mm resected colorectal liver metastasis demonstrating peripheral viable tumour with a centrally necrotic region. In image B the $\mathrm{ROI}_{\text{lesion-histopathology}}$ is outlined (black line) and the regions $\mathrm{ROI}_{\text{viable-histopathology}}$ (solid grey region) and $\mathrm{ROI}_{\text{nonviable-histopathology}}$ (shaded grey region) are shown.

Figure 2:

Two-stage semi-automated segmentation of manually delineated liver metastasis by PCA clustering based on DCE-MRI signal-time curves. Image 2a and 2c show the four automatically defined subregions within $\mathrm{VOI}_{\text{lesion-imaging}}$ and images 2b and 2d show the four mean signal-time curves for the equivalent regions. The three wash-in wash-out curves (Image 2b, labels 1, 2 and 4) were merged to create $\mathrm{VOI}_{\text{viable-imaging-subregion}}$ while the remaining voxels are classified as $\mathrm{VOI}_{\text{nonviable-imaging-subregion}}$.

Figure 3:

Image 3a shows the spatial overlap of $ROI_{lesion\text{-}histopathology}$ (green outline) and $ROI_{lesion\text{-}imaging}$ (red outline). Image 3b shows the spatial overlap of $ROI_{viable\text{-}histopathology}$ (between outer green outline and inner red outline) and $ROI_{viable\text{-}imaging\text{-}subregion}$ (between outer green and inner green outline; derived from $ROI_{lesion\text{-}histopathology}$). Dice similarity coefficients were 0.834 and 0.93, respectively.

Figure 4:

Mean K^{trans} of colorectal liver metastases (dark blue) image VOIs and of image-derived tumour (purple) and non-tumour subregions (green).

Figure 5:

Mean k_{ep} of colorectal liver metastases (dark blue) image VOIs and of image-derived tumour (purple) and non-tumour subregions (green).

Figure 6:

Image 6a is a resected colorectal liver metastasis with central non-viable tumour (NV) and a rim of viable (V) tumour. Image 6b is the K^{trans} map for the whole lesion and Image 6b is the K^{trans} map for the viable tumour subregion only.

Table 1

Table 1*:* Dice similarity coefficients comparing $\mathrm{ROI}_{\text{lesion-histopathology}}$ with $\mathrm{ROI}_{\text{lesion-imaging,}}$ and comparing $\mathrm{ROI}_{\text{viable-imaging-subregion}}$ with $\mathrm{ROI}_{\text{viable-histopathology}}$

Patient Number	**Pixels in $\mathrm{ROI}_{\text{lesion}}$**	**$\mathrm{ROI}_{\text{lesion}}$**	**$\mathrm{ROI}_{\text{viable}}$**
001	520	NA (interval chemotherapy)	
002	445	0.923	0.784
003	197	0.872	0.831
004	275	0.909	0.734
005	1253	0.834	0.930
006	661	0.746	0.635
007	987	NA (complete pathological response)	
008	1502	0.952	0.784
010	479	0.769	0.663
011	1052	NA (recurrent tumour)	
012	320	NA (interval chemotherapy)	
013	1342	0.885	0.737
014	2869	NA (abandoned metastasectomy)	
015	148	0.782	0.540
Mean	861	**0.852**	**0.738**
Standard Deviation	731	**0.073**	**0.115**

Table 2

Table 2: Proportion of viable tumour (%) by visual assessment of the histopathology, and calculated from the histopathology-defined and imaging-derived subregions.

Patient	Histopathology Visual Assessment (%)	Histopathology Subregions (%)	Imaging ROI Subregions (%)	Imaging VOI Subregions (%)
001pre	NA (interval chemotherapy)		68	69
002	15	50	27	38
003	30	66	76	74
004	35	58	52	47
005	50	77	85	87
006	30	46	100	100
007pre	NA (complete pathological response)		72	80
008	30	51	47	44
010pre	NA (interval chemotherapy)		42	46
010post	5	45	59	62
011	10	.	25	27
012pre	NA (interval chemotherapy)		39	59
013	30	49	34	35
014	NA (abandoned metastasectomy)		42	48
015	50	54	73	70
Mean	31.7	55.1	56.1	59.1
Standard Deviation	11.3	10.5	22.2	20.8

Figure 1

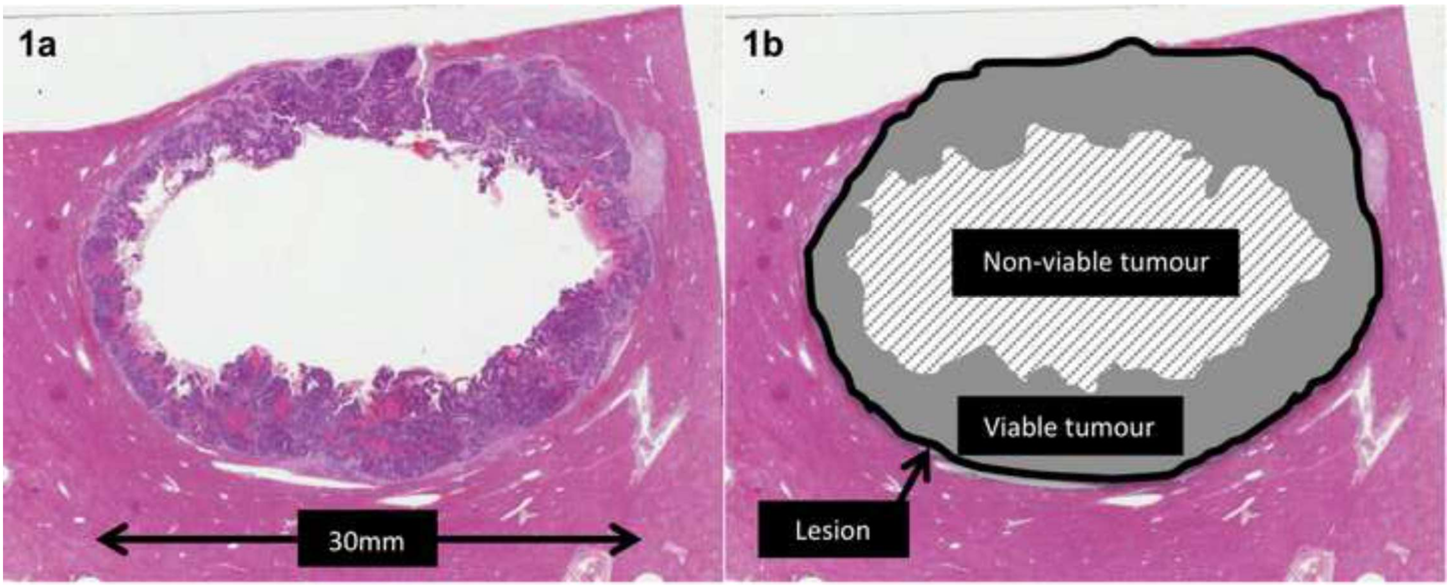

Figure 2

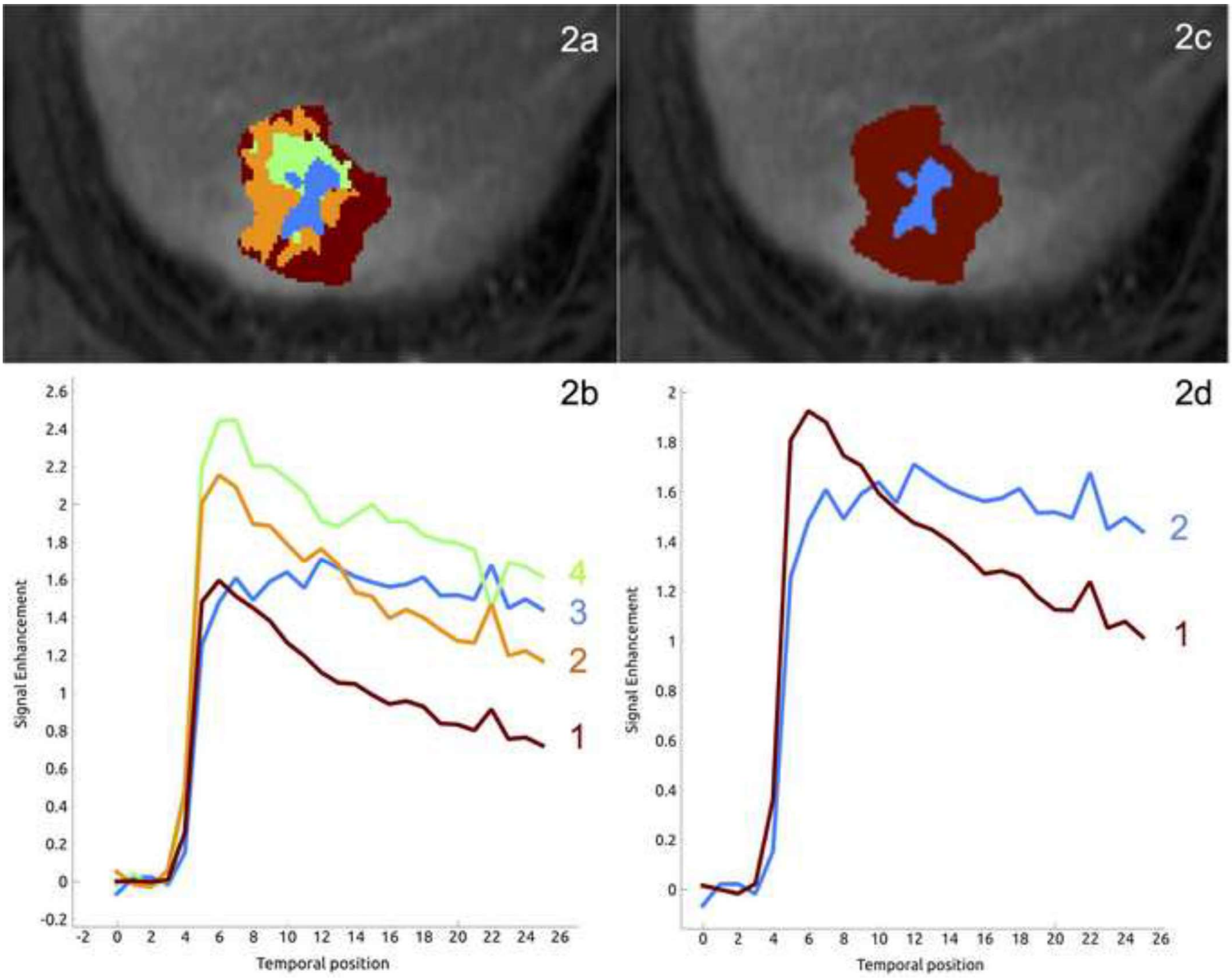
2a
2c
2b
2d
Signal Enhancement
Temporal position
2.6
2.4
2.2
2
1.8
1.6
1.4
1.2
1
0.8
0.6
0.4
0.2
0
-0.2
-2
0
2
4
6
8
10
12
14
16
18
20
22
24
26
4
3
2
1
Signal Enhancement
Temporal position
2
1.8
1.6
1.4
1.2
1
0.8
0.6
0.4
0.2
0
0
2
4
6
8
10
12
14
16
18
20
22
24
26
2
1

Figure 3

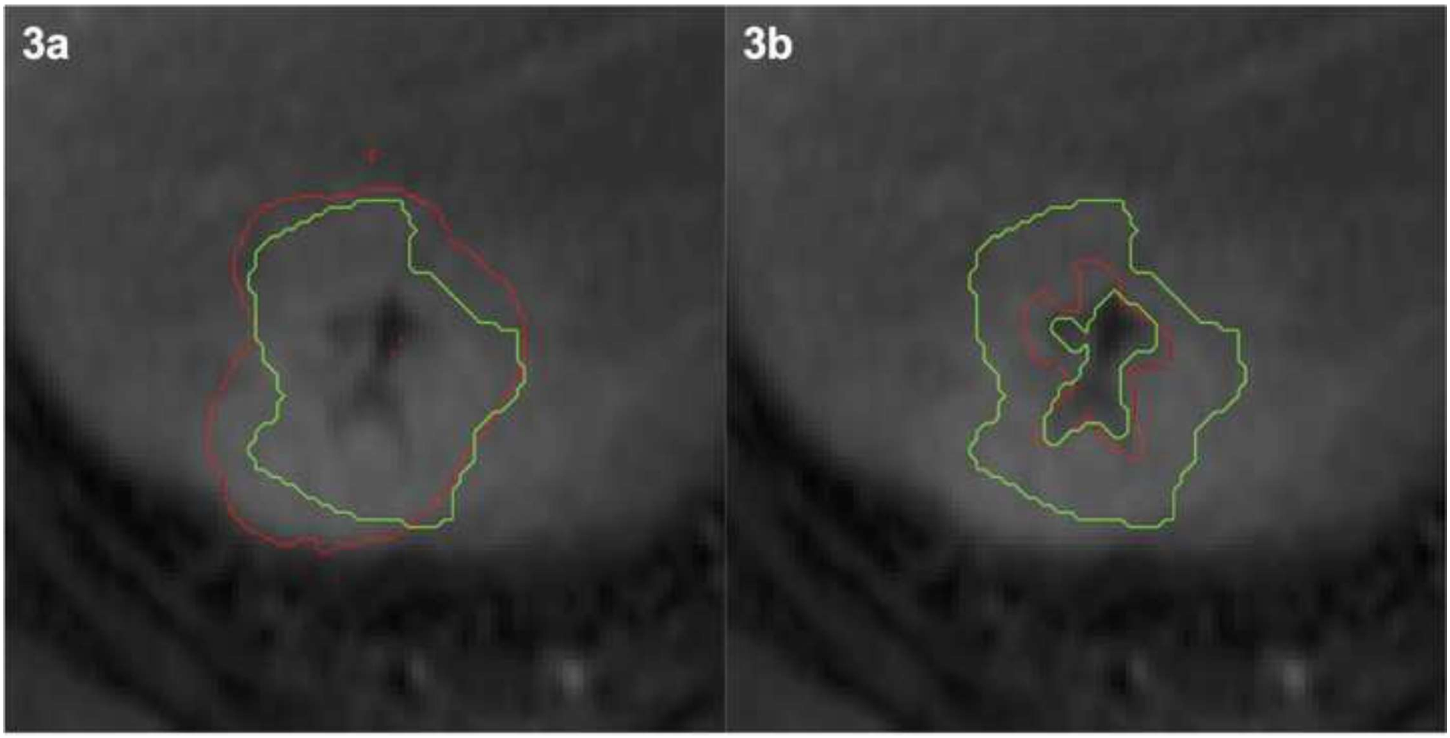

Figure 4

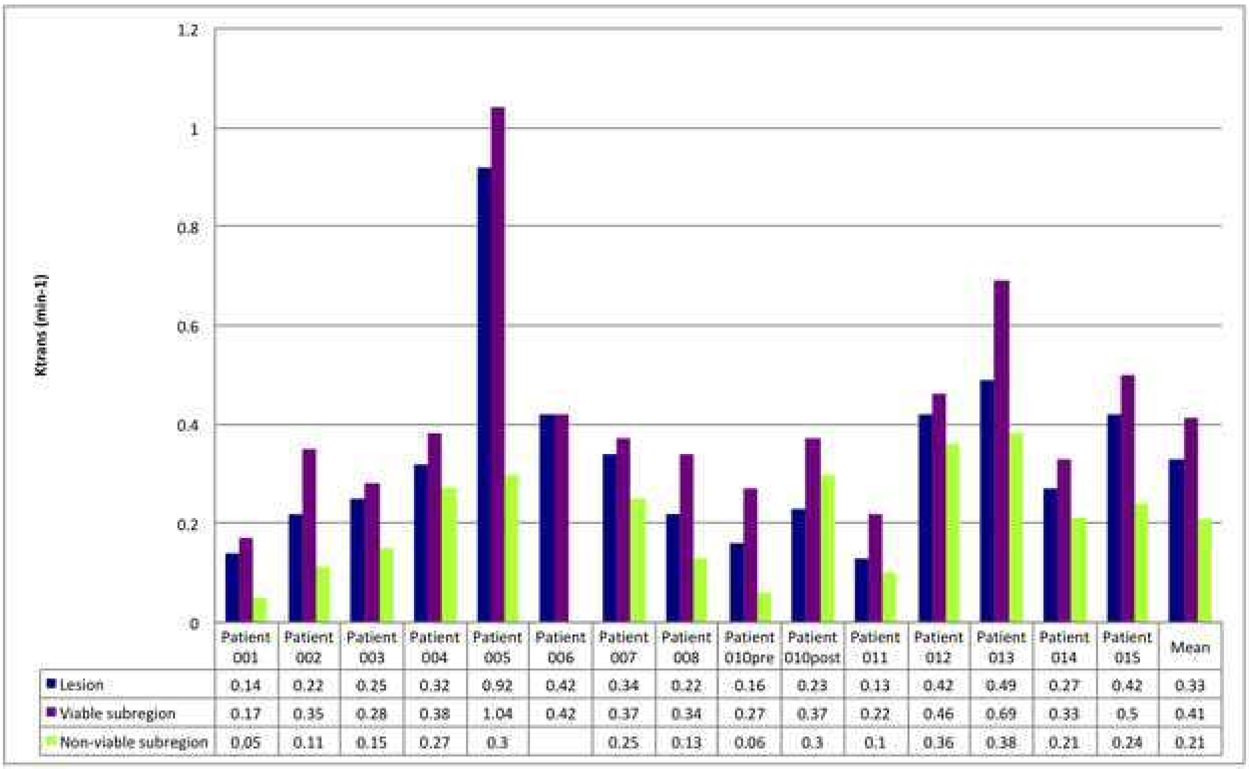

	Patient 001	Patient 002	Patient 003	Patient 004	Patient 005	Patient 006	Patient 007	Patient 008	Patient 010pre	Patient 010post	Patient 011	Patient 012	Patient 013	Patient 014	Patient 015	Mean
■ Lesion	0.14	0.22	0.25	0.32	0.92	0.42	0.34	0.22	0.16	0.23	0.13	0.42	0.49	0.27	0.42	0.33
■ Viable subregion	0.17	0.35	0.28	0.38	1.04	0.42	0.37	0.34	0.27	0.37	0.22	0.46	0.69	0.33	0.5	0.41
■ Non-viable subregion	0.05	0.11	0.15	0.27	0.3		0.25	0.13	0.06	0.3	0.1	0.36	0.38	0.21	0.24	0.21

Figure 5

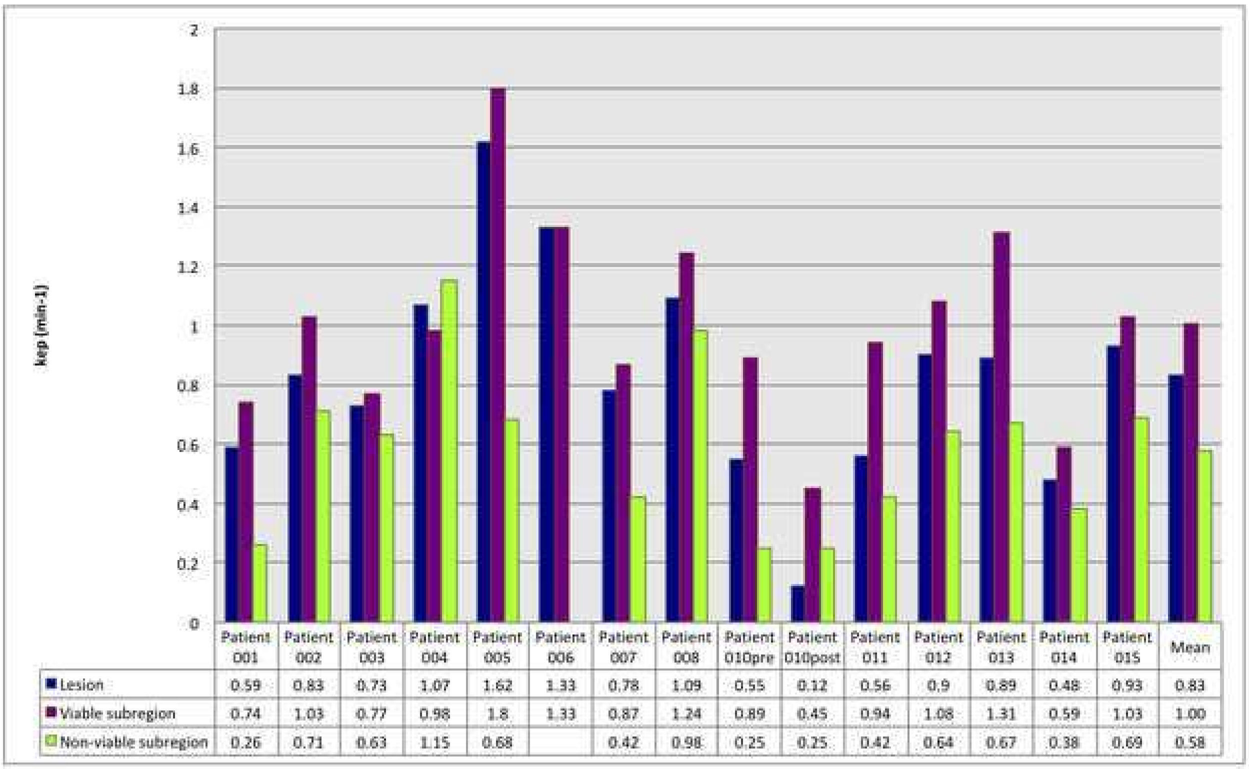

	Patient 001	Patient 002	Patient 003	Patient 004	Patient 005	Patient 006	Patient 007	Patient 008	Patient 010pre	Patient 010post	Patient 011	Patient 012	Patient 013	Patient 014	Patient 015	Mean
■ Lesion	0.59	0.83	0.73	1.07	1.62	1.33	0.78	1.09	0.55	0.12	0.56	0.9	0.89	0.48	0.93	0.83
■ Viable subregion	0.74	1.03	0.77	0.98	1.8	1.33	0.87	1.24	0.89	0.45	0.94	1.08	1.31	0.59	1.03	1.00
🟩 Non-viable subregion	0.26	0.71	0.63	1.15	0.68		0.42	0.98	0.25	0.25	0.42	0.64	0.67	0.38	0.69	0.58

Figure 6